Electronic Supplementary Material (ESI) for Journal of Materials Chemistry A.

Electronic Supplementary Information

Stepped surface-rich copper fiber felt as an efficient electrocatalyst for CO_2RR to formate

Sibo Shen†, Jia He†, Xianyun Peng†, Wei Xi, Lihan Zhang, Desheng Xi, Lei Wang, Xijun Liu*, Jun Luo*

Center for Electron Microscopy and Tianjin Key Lab of Advanced Functional Porous Materials, Institute for New Energy Materials & Low-Carbon Technologies, School of Materials Science and Engineering, Tianjin University of Technology, Tianjin 300384, People's Republic of China

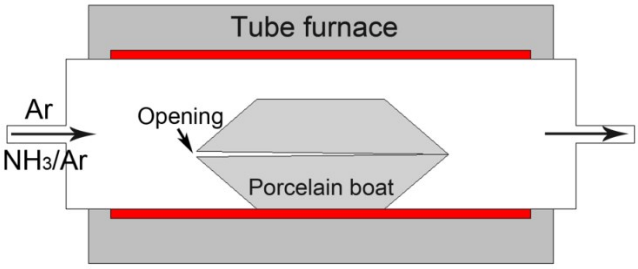

Figure S1 Schematic illustration of the synthetic apparatus for Cu fiber felt.

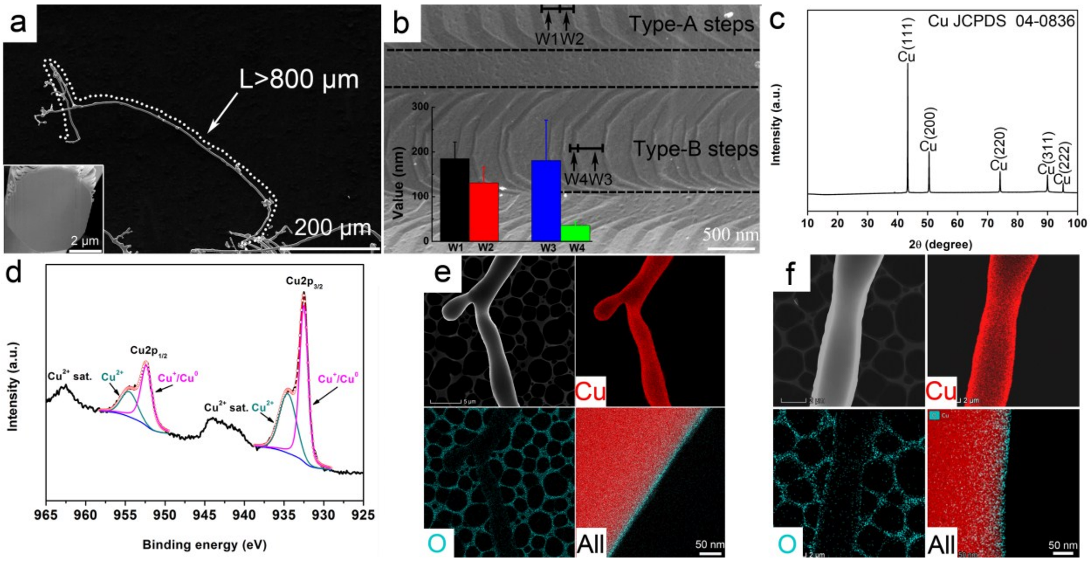

Figure S2 (a) Low-magnification SEM image of surface morphology of a Cu fiber with the length of more than 800 μm, and its inset shows the typical cross-section morphology of a Cu fiber after FIB cutting. (b) High-magnification SEM image of surface morphology of Type-A steps and Type-B steps (the inset shows the width distribution chart of the two types of steps). (c) XRD pattern of Cu fiber felt. (d) Cu 2P XPS spectrum of Cu fiber felt. (e) High angle annular dark-field (HAADF) STEM image of a Cu fiber and its EDS elemental mapping of Cu and O. (f) HAADF STEM image and the EDS elemental mapping of Cu and O of a Cu fiber, which was etched in 1 M HNO_3 for 30 s, followed by rinsed in deionized water and alcohol, and dried in N_2 gas (the etched Cu fiber).

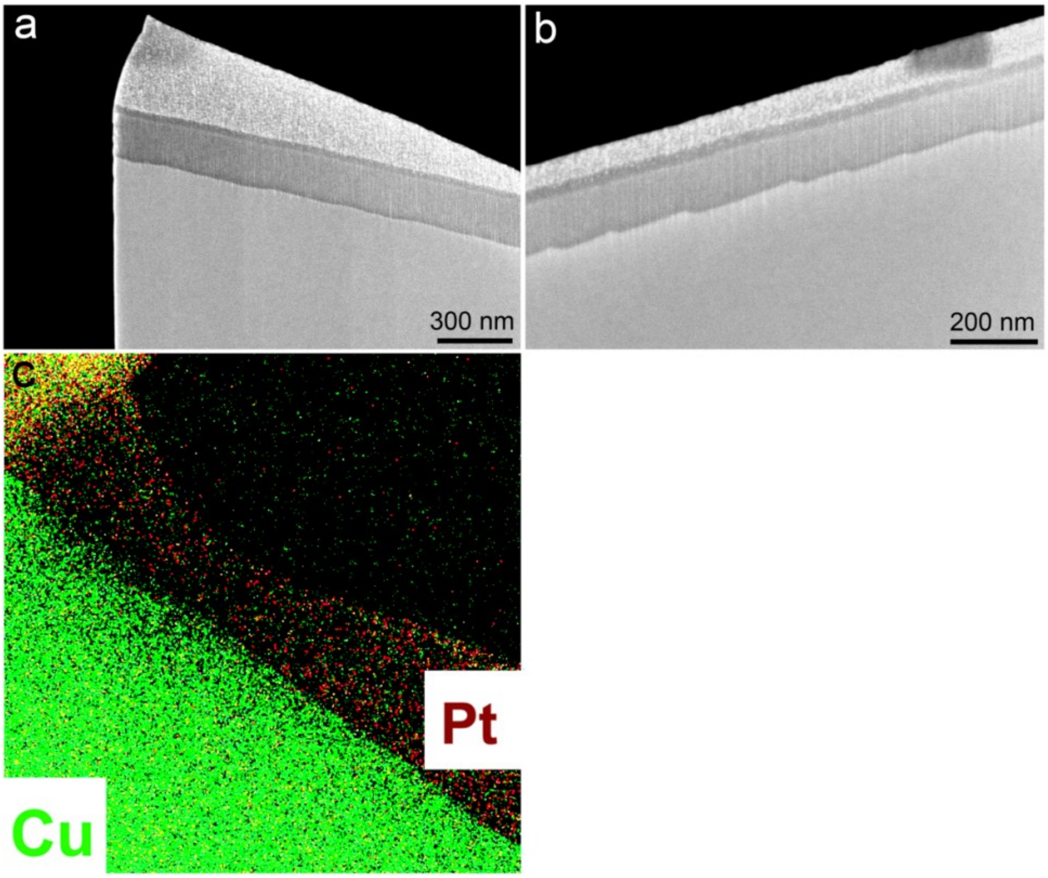

Figure S3 SEM image of cross-section morphologies of the stepped surfaces on Cu fiber: (a) Type-A steps; (b) Type-B steps. (c) The EDS elemental mapping of Cu and Pt elements for Figure 2a.

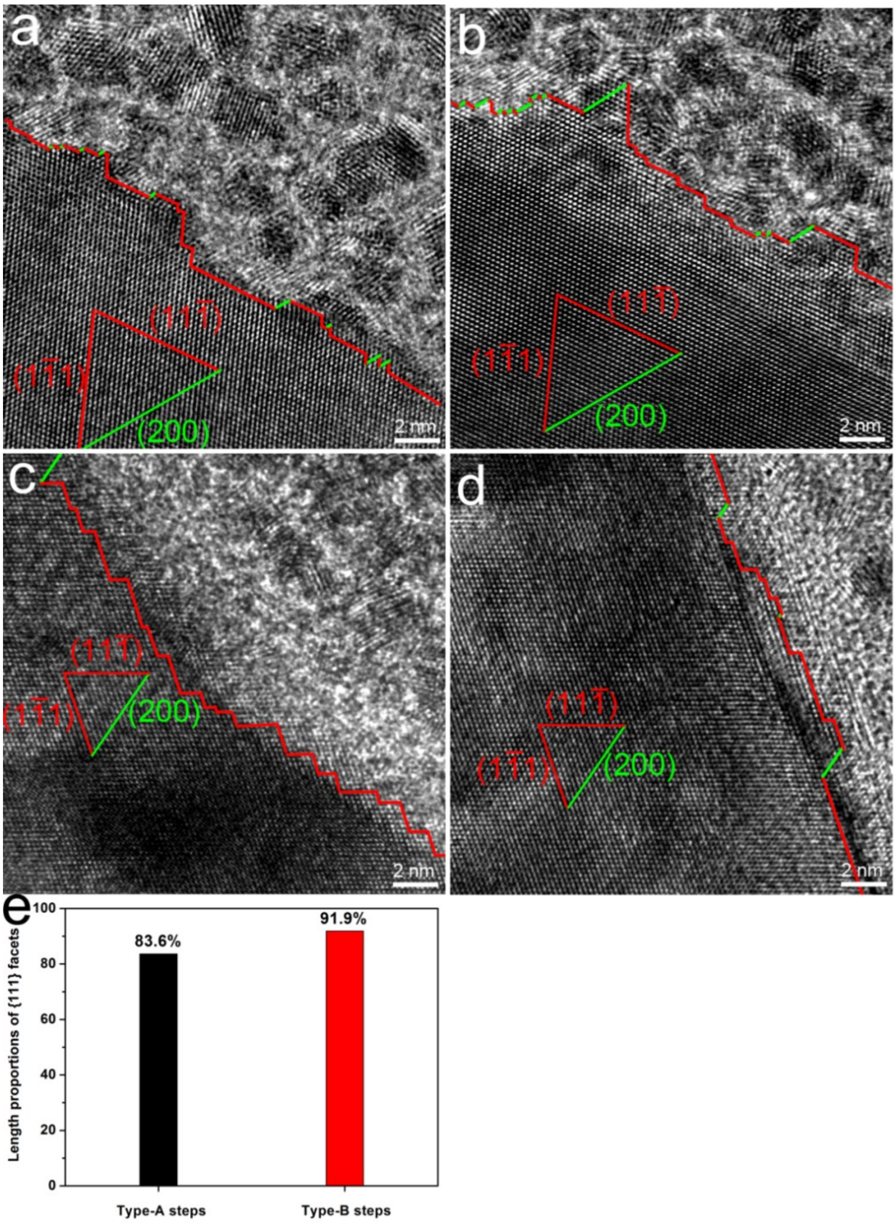

Figure S4 (a, b) TEM images of cross-section morphologies of two additional locations on Type-A steps. (c, d) TEM images of cross-section morphologies of two additional locations on Type-B steps. (e) Length proportions of {111} facets for Type-A steps and Type-B steps, respectively. In order to quantitatively analyze the length proportions of {111} facets for the two types of steps, two additional locations were randomly selected from Type-A steps and Type-B steps, respectively. Then, we counted the lengths of {111} facets and {100} facets from Figures S4a, b and 2b, c for Type-A steps, and these from Figures S4c, d and 2e, f for Type-B steps. Finally, the proportions of {111} facets to the total facets for the two types of steps were calculated and the results are shown in Figure S4e.

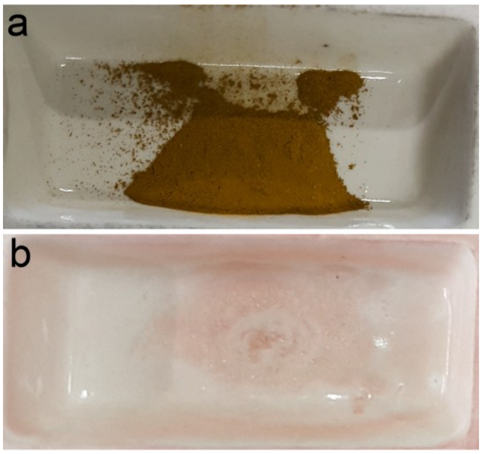

Figure S5 Optical images of (a) the raw material of Sample I and (b) Sample I.

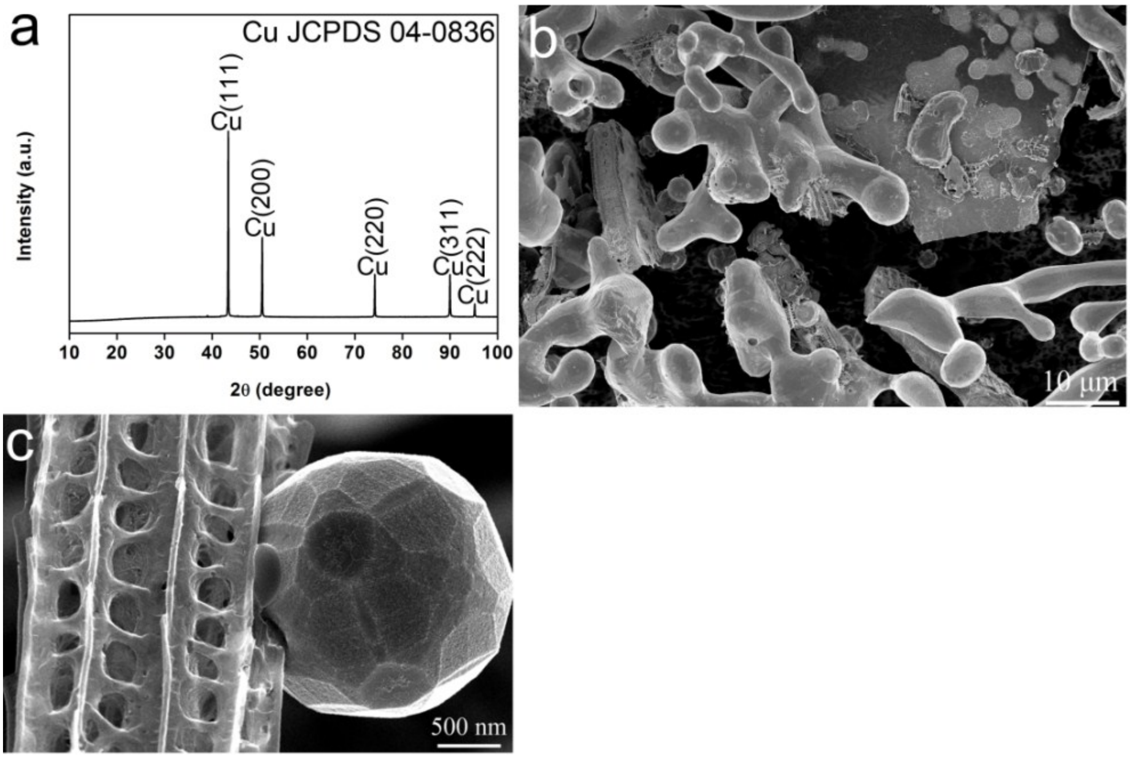

Figure S6 (a) XRD pattern of Sample III. (b) SEM image of surface morphology of Sample III. (c) SEM image of a representative Cu particle anchored on the skeleton of a CBW. The XRD pattern in Figure S6a shows the existence of only Cu diffraction peaks of (111), (200), (220), (311) and (222), proving metallic Cu material is obtained for Sample III.

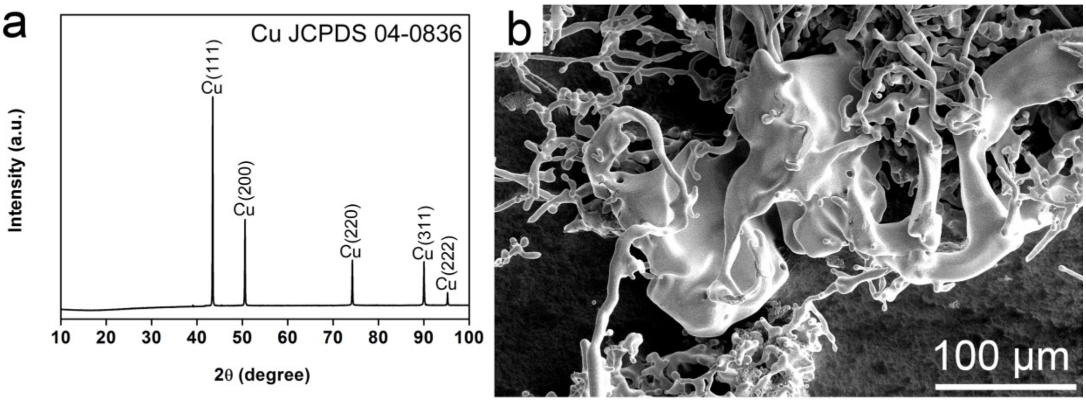

Figure S7 (a) XRD pattern of Sample V. (b) SEM image of surface morphology of Sample V. The XRD pattern in Figure S7a shows the existence of only Cu diffraction peaks of (111), (200), (220), (311) and (222), proving metallic Cu material is obtained for Sample V.

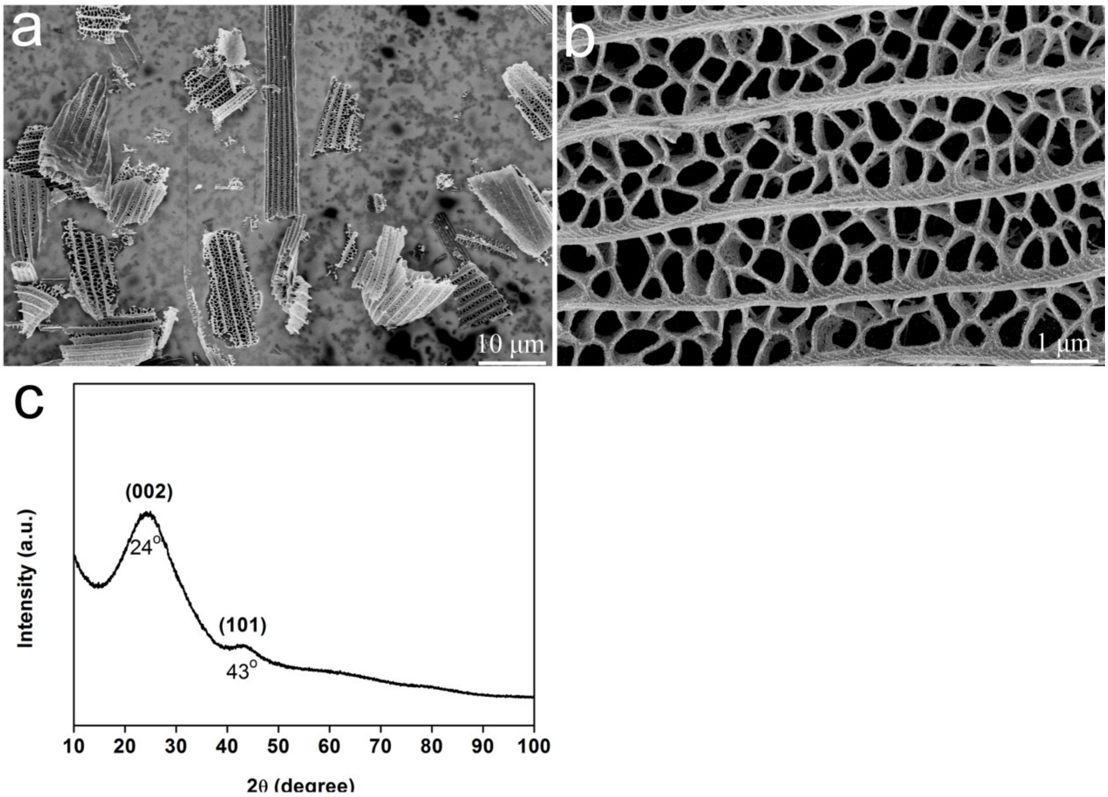

Figure S8 (a, b) Low- and high-magnification SEM images of surface morphologies of Sample IV. (c) XRD pattern of Sample IV.

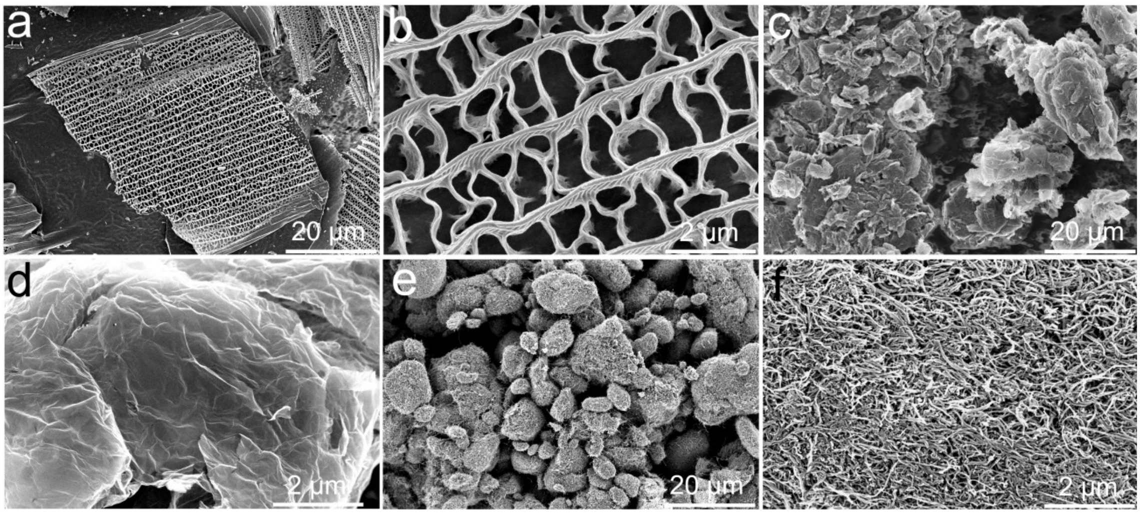

Figure S9 (a, b) Low- and high-magnification SEM images of surface morphologies of CBWs. (c, d) Low- and high-magnification SEM images of surface morphologies of graphenes. (e, f) Low- and high-magnification SEM images of surface morphologies of MWCNTs.

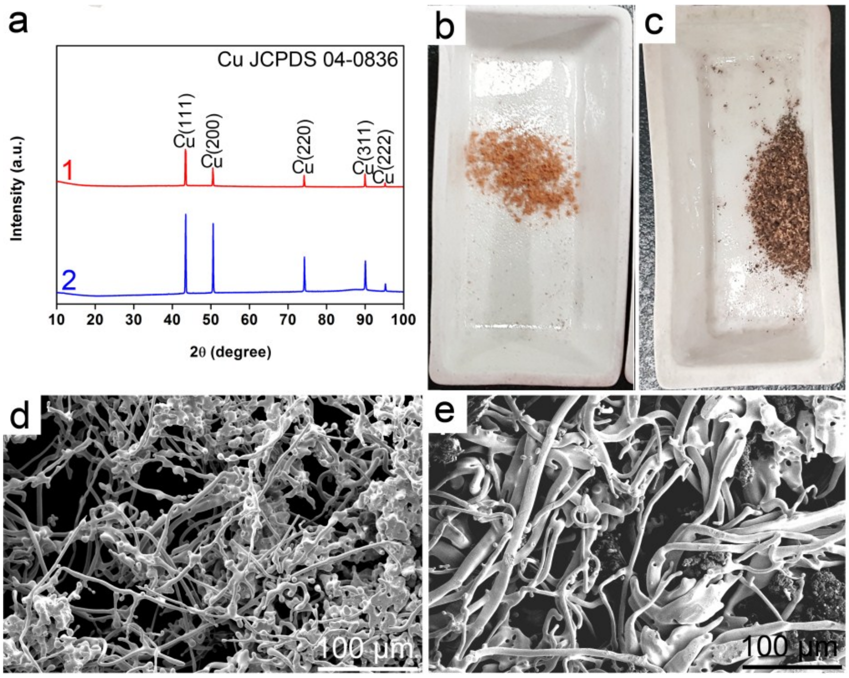

Figure S10 (a) XRD patterns of (1) Sample VI and (2) Sample VII. Optical images of (b) Sample VI and (c) Sample VII. SEM images of surface morphologies of (d) Sample VI and (e) Sample VII. The XRD patterns in Figure S10a show the existence of only Cu diffraction peaks of (111), (200), (220), (311) and (222), proving metallic Cu material is obtained for both Sample VI and Sample VII. The optical images (Figure S10b, c) present that both Sample VI and Sample VII are composed of incompact granules, so they don't exhibit the felt structure. Compared with Cu fiber felt, although the SEM images (Figure S10d, e) demonstrate that both Sample VI and Sample VII also consist of micron-scale Cu fibers, but the fibers are not enough to form the felt. The contents of Cu fibers in the samples are mainly ascribed to the structure of the applied templates. Comparatively, CBW has intrinsic submicron-scale pores within its skeleton (Figure S9a, b), which benefit the capture of the floating Cu particles and further facilitate Cu fiber felt formation. However, neither graphene nor MWCNT has submicron-scale pores (Figure S9c, d, e, f), so they cannot effectively capture the floating Cu particles. Overall, both graphene and MWCNT are not effective templates for the synthesis of Cu fiber felt.

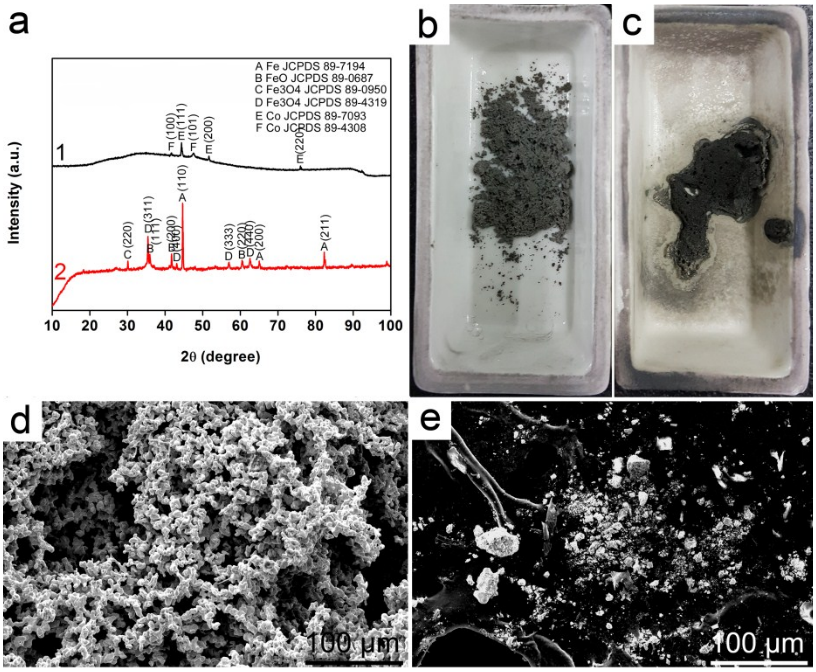

Figure S11 (a) XRD patterns of (1) Sample VIII and (2) Sample IX. Optical images of (b) Sample VIII and (c) Sample IX. SEM images of surface morphologies of (d) Sample VIII and (e) Sample IX. In this work, we attempted to adopt this template strategy to synthesize cobalt (Co) or iron (Fe) felt-like materials using $CoCl_2·6H_2O$ and $FeCl_3$ as metal precursors, respectively. The proportion of $CoCl_2·6H_2O$ to CBWs for Co material, and the proportion of $FeCl_3$ to CBWs for Fe material were set in accordance with that for Cu fiber felt (the amounts of Co and Fe in their raw materials were identical with that of Cu for Cu fiber felt). In detail, 0.237 g $CoCl_2·6H_2O$ and 0.012 g CBWs were employed; 0.162 g $FeCl_3$ and 0.012 g CBWs were employed. The whole synthetic processes for Co and Fe materials were identical with that for Cu fiber felt. The samples synthesized using $CoCl_2·6H_2O$ and CBWs, and $FeCl_3$ and CBWs as raw materials are denoted as **Sample VIII** and **Sample IX**, respectively. The XRD patterns in Figure S11a show that a single-phase metallic Co is produced for Sample VIII; however, multi-phase Fe, FeO and Fe_3O_4 mixture is produced for Sample IX. Moreover, Sample VIII demonstrates a kind of micron-scale porous structure, which is constructed by Co particles connection (Figure S11b, d), in parallel, Sample IX is composed of random particles (Figure S11c, e).

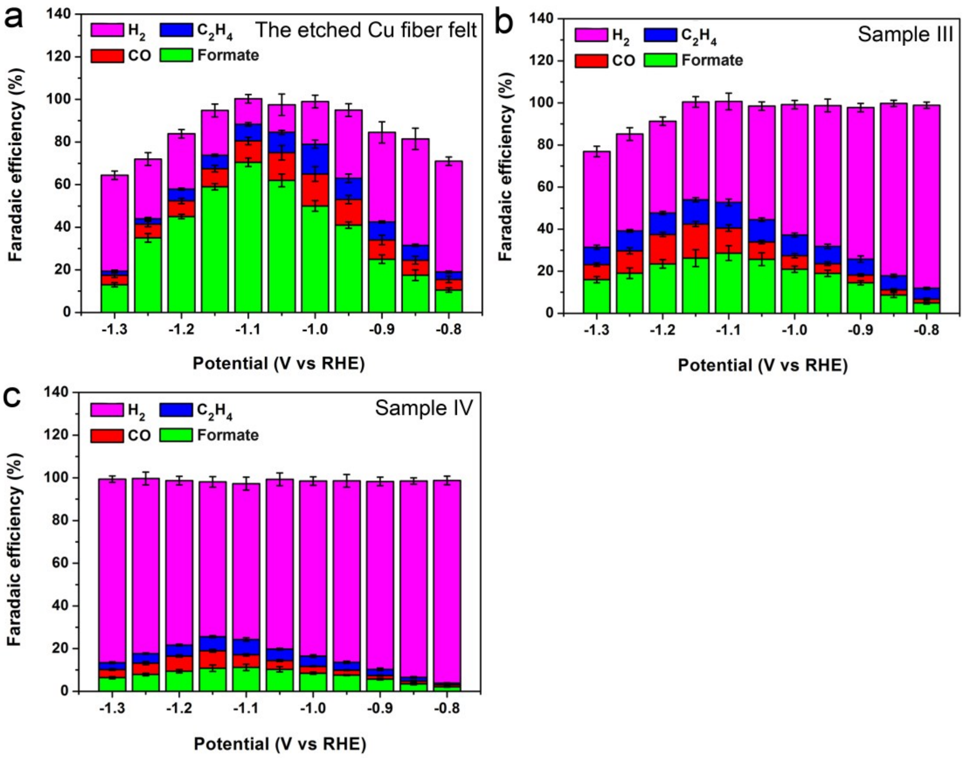

Figure S12 FEs of formate, CO, C_2H_4 and H_2 on (a) the etched Cu fiber felt (b) Sample III and (c) Sample IV, at different applied potentials.

Table S1 FE of formate (formic acid) and its stability on Cu electrocatalysts for CO_2RR reported in this work and other literatures.

Catalyst	Electrolyte	FE_{max} %	E_{max}	Stability h	Ref.
Cu fiber felt	0.1 M $KHCO_3$	71.1	−1.1 V_{RHE}	6.7	This work
Porous dendritic Cu	EMIM(BF_4)[a]/H_2O (92/8 v/v)	83	−1.55 V vs Fc_+/Fc[b]	8	S1
500 °C annealed and electrochemically reduced Cu foam	0.1 M $KHCO_3$	*ca.* 23	−0.45 V_{RHE}	N.R.	S2
500 °C annealed and electrochemically reduced Cu foil	0.1 M $KHCO_3$	*ca.* 38	−0.55 V_{RHE}	7	S3
CuO derived Cu nanowire arrays on Cu foil	0.1 M $KHCO_3$	*ca.* 20	−0.7 to −1.1 V_{RHE}	N.R.	S4
500 °C annealed and electrochemically reduced Cu nanowires on Cu mesh	0.1 M $KHCO_3$	30.7	−0.595 V_{RHE}	1	S5
Porous hollow fiber Cu	0.3 M $KHCO_3$	*ca.* 25	−0.3 V_{RHE}	0.5	S6
Electropolished Cu foil	0.1 M $KHCO_3$	*ca.* 24	−0.85 V_{RHE}	N.R.	S7
O_2 plasma-activated Cu foil	0.1 M $KHCO_3$	*ca.* 23	−0.60 V_{RHE}	N.R.	
Electropolished Cu	0.1 M $KHCO_3$	12.76	−0.99 V_{RHE}	N.R.	S8
Cu_2O film with thickness of 0.2 µm	0.1 M $KHCO_3$	12.67	−0.99 V_{RHE}	N.R.	
Cu foil	0.1 M $CsHCO_3$	30.9	−0.7 V_{RHE}	N.R.	S9
Oxide-derived Cu	0.1 M $CsHCO_3$	8.80	−0.7 V_{RHE}	N.R.	
Electrochemically cycled Cu	0.1 M $CsHCO_3$	14.3	−0.7 V_{RHE}	N.R.	
Cu foil	0.1 M $KHCO_3$	17.0	−0.7 V_{RHE}	N.R.	
Oxide-derived Cu	0.1 M $KHCO_3$	13.8	−0.7 V_{RHE}	N.R.	
Electrochemically cycled Cu	0.1 M $KHCO_3$	18.4	−0.7 V_{RHE}	N.R.	
5-fold twinned Cu nanowire	0.1 M $KHCO_3$	*ca.* 21	−0.96 V_{RHE}	N.R.	S10
Cu_2O-derived Cu	0.1 M $KHCO_3$	24.95	−0.78 V_{RHE}	N.R.	S11
Cu(100) single crystal	0.1 M $KHCO_3$	9.02	−0.85 V_{RHE}	N.R.	
Cu(111) single crystal	0.1 M $KHCO_3$	20.83	−0.95 V_{RHE}	N.R.	
Cu(110) single crystal	0.1 M $KHCO_3$	24.71	−0.8 V_{RHE}	N.R.	
Electropolished Cu sponge	0.5 M $NaHCO_3$	28	−0.8 V_{RHE}	N.R.	S12
Annealed Cu sponge	0.5 M $NaHCO_3$	34	−0.8 V_{RHE}	N.R.	
Electrodeposited Cu sponge	0.5 M $NaHCO_3$	24	−0.7 V_{RHE}	N.R.	
Cu foil	0.5 M $NaHCO_3$	*ca.* 19	−1.1 V_{RHE}	N.R.	

Electrodeposited Cu nanofoam	0.1 M $KHCO_3$	37	−1.5 $V_{Ag/AgCl}$	N.R.	S13

[a]EMIM(BF_4) is short for 1-ethyl-3-methylimidazolium tetra-fluoroborate. [b]–1.55 V vs Fc^+/Fc: this electrochemical applied potential of –1.55 V is vs Fc^+/Fc; the other potentials are vs RHE. [c]N.R.: not reported.

Supporting References

S1. T. N. Huan, P. Simon, G. Rousse, I. Génois, V. Artero and M. Fontecave, *Chem. Sci.*, 2017, **8**, 742–747.

S2. S. X. Min, X. L. Yang, A. Lu, C. Tsend, M. N. Hedhili, L. Li and K. Huang, *Nano Energy*, 2016, **27**, 121–129.

S3. C. W. Li and M. W. Kanan, *J. Am. Chem. Soc.*, 2012, **134**, 7231–7234.

S4. M. Ma, K. Djanashvili and W. A. Smith, *Angew. Chem. Int. Ed*. 2016, **55**, 6680–6684.

S5. D. Raciti, K. J. Livi and C. Wang, *Nano Lett*., 2015, **15**, 6829–6835.

S6. R. Kas, K. K. Hummadi, R. Kortlever, P. Wit, A. Milbrat, M. W. J. Luiten-Olieman, N. E. Benes, N. E. Benes, M. T. M. Koper and G. Mul, *Nat. Commun*., 2016, **7**, 10748–10754.

S7. H. Mistry, A. S. Varela, C. S. Bonifacio, I. Zegkinolou, I. Sinev, Y. Choi, K. Kisslinger, E. A. Stach, J. C. Yang, P. Strasser and B. R. Cuenya, *Nat. Commun*., 2016, **7**, 12123–12131.

S8. D. Ren, Y. L. Deng, A. D. Handoko, C. S. Chen, S. Malkhandi and B. S. Yeo, *ACS Catal*., 2015, **5**, 2814–2821.

S9. P. Huang, S. Q. Ci, G. X. Wang, J. C. Jia, J. W. Xu, Z. H. Wen, *J. CO2 Util.,* 2017, **20**, 27–33.

S10. Y. F. Li, F. Cui, M. B. Ross, D. Kim, Y. C. Sun and P. D. Yang, *Nano Lett*., 2017, **17**, 1312–1317.

S11. Y. Huang, A. D. Handoko, P. Hirunsit and B. S. Yeo, *ACS Catal.*, 2017, **7**, 1749–1756.

S12. A. Dutta, M. Rahaman, M. Mohos, A. Zanetti and P. Broekmann, *ACS Catal.*, 2017, **7**, 5431–5437.

S13. S. Sen, D. Liu and G. T. R. Palmore, *ACS Catal.*, 2014, **4**, 3091–3095.